photonics

MDPI

Article

Nonlocal Interactions in Metasurfaces Harnessed by Neural Networks

Yongle Zhou [1], Qi Xu [1], Yikun Liu [2], Emiliano R. Martins [3], Haowen Liang [1,4,*] and Juntao Li [1,4,*]

[1] State Key Laboratory of Optoelectronic Materials and Technologies, School of Physics, Sun Yat-sen University, Guangzhou 510275, China; zhouyle@mail2.sysu.edu.cn (Y.Z.); xuqi8@mail2.sysu.edu.cn (Q.X.)
[2] Guangdong Provincial Key Laboratory of Quantum Metrology and Sensing, School of Physics and Astronomy, Sun Yat-Sen University, Zhuhai 519080, China; liuyk6@mail.sysu.edu.cn
[3] São Carlos School of Engineering, Department of Electrical and Computer Engineering, University of São Paulo, São Carlos 13566-590, SP, Brazil; erm@usp.br
[4] Quantum Science Center of Guangdong-Hong Kong-Macao Greater Bay Area (Guangdong), Shenzhen 518045, China
* Correspondence: lianghw26@mail.sysu.edu.cn (H.L.); lijt3@mail.sysu.edu.cn (J.L.)

Abstract

Optical metasurfaces enable compact, lightweight and planar optical devices. Their performances, however, are still limited by design approximations imposed by their macroscopic dimensions. To address this problem, we propose a neural network-based multi-stage gradient optimization method to efficiently modulate nonlocal interactions between meta-atoms, which is one of the major effects neglected by current design methods. Our strategy allows for the use of these interactions as an additional design dimension to enhance the performance of metasurfaces and can be used to optimize large-scale metasurfaces with multiple parameters. As an example of application, we design a meta-hologram with a zero-order energy suppressed to 26% (theoretically) and 57% (experimentally) of its original value. Our results suggest that neural networks can be used as a powerful design tool for the next generation of high-performance metasurfaces with complex functionalities.

Keywords: nonlocal interactions; meta-hologram; neural network; zero-order

Received: 28 June 2025
Revised: 14 July 2025
Accepted: 17 July 2025
Published: 19 July 2025

Citation: Zhou, Y.; Xu, Q.; Liu, Y.; Martins, E.R.; Liang, H.; Li, J. Nonlocal Interactions in Metasurfaces Harnessed by Neural Networks. *Photonics* **2025**, *12*, 738. https://doi.org/10.3390/photonics12070738

1. Introduction

Metasurfaces offer versatile control of light beams in multiple dimensions, enabling advanced optical functionalities such as metalenses [1–4], meta-holograms [5–7] and other unique applications [8,9]. Even though there has been impressive progress in fundamental research and applications, metasurface designs are still largely based on selecting meta-atoms from a predefined library to modulate the phase at specific positions [10,11]. This method provides a fast approach to design metasurfaces of macroscopic dimensions by assuming that the optical properties of each meta-atom are the same in the metasurfaces as they are in a periodic array (the so-called local periodic approximation). The downside of the standard method is that it overlooks nonlocal effects [11], including interactions between meta-atoms and leaky modes, thus limiting optical performance [12,13]. Furthermore, nonlocal effects can enable unique functionalities, such as wavelength selection [14,15], wavefront selection [16] and image processing [17,18]. Thus, there is a pressing need to develop practical design strategies to control nonlocal effects.

Recently, inverse design methods such as adjoint-based optimization [19,20] have been proposed to address these issues by incorporating nonlocal effects to adjust the complex

amplitude of the meta-atoms, thus improving the design of phase-matching metasurfaces. Despite their benefits, these approaches have important limitations. For example, adjoint-based optimization requires full-structure simulations, making it computationally expensive and unsuitable for large-scale devices [21–23]. The supercell method [24,25] simplifies the design of specific devices, but it is cumbersome if complex functionalities are to be accommodated. Deep learning methods have emerged as an alternative, enabling rapid predictions of wavefront outputs by learning meta-atom responses under nonlocal interactions [26–29]. Moreover, the direct generation capability of generative neural networks for structural design also provides a new perspective [30]. However, due to a strong dependence on the dataset, this method is not easy to extend to other types of metasurfaces, resulting in poor scalability. Additionally, the gradient optimization techniques based on differentiable calculations utilize the prediction capability of neural network models to design large-scale metasurfaces with different functions [31–33]. However, challenges such as limited optimization parameters and gradient calculation errors from discrete datasets still constrain device performance and functionality.

Here, we propose a new neural network-based multi-stage gradient optimization strategy to modulate nonlocal interactions between meta-atoms. Currently, there are two main approaches to optimize metasurface structures and mitigate nonlocal effects. One approach, which is adopted here, takes the ideal performance of the metasurfaces as the optimization target [23,31]. The other approach uses the actual phase response of the metasurfaces as the optimization target [28]. Our strategy is based on a decomposition of a multi-parameter optimization into sequential stages, with each stage employing a neural network trained on continuous parameter variations. This approach reduces data requirements and minimizes errors caused by discrete datasets, enabling optimization of more parameters. Additionally, discretization methods are incorporated to ensure the optimized structure meets fabrication requirements, significantly enhancing the practicality of gradient optimization. As an example, we apply this method to optimize meta-holograms for zero-order suppression, achieving a reduction to 26% (theoretically) and 57% (experimentally) of the original zero-order energy. Compared to conventional solutions such as off-axis design strategies [5], polarization detection methods [34,35], or supercell approaches [36], our approach avoids limitations like reduced imaging range, lower efficiency, or increased system complexity. We believe that this method offers a promising route to design large-scale complex metasurfaces and effectively modulate nonlocal effects.

2. Method

Neural network-based gradient optimization methods for metasurface design typically rely on a single network model to optimize parameters. When using a dataset with continuous parameters for training, the increased complexity of the dataset often limits these parameters to the diameters of the meta-atoms' nanopillars, which restricts the optimization scope and effectiveness. Additionally, the optimized structural parameters are often not compatible with conventional fabrication techniques. To increase the range of optimizable parameters, for example, by varying the position of the nanopillars within the meta-atoms, datasets with only preset discrete values are often used for training. However, the lack of data between these discrete values leads to calculation errors in the continuous gradient, which negatively impacts the optimization outcome.

Here, we use multiple Prediction Neural Network (PNN) models to independently optimize different parameters, with each model learning the continuous dataset for its respective parameters. This strategy improves gradient accuracy and enables optimization of additional parameters. The optimization process is divided into coarse and fine adjustment

stages and combined with discretization methods to stay within the range compatible with fabrication requirements.

As an example of application, we optimize a meta-hologram to suppress its zero-order energy. Compared to traditional holograms, meta-holograms offer smaller device sizes, wider Field of View (FoV) and higher efficiency, making them more suitable for applications in information storage [37–39] and optical encryption [40,41]. However, their imaging quality is often degraded by the zero-order component [5,34]. Theoretically, the zero-order component vanishes in an ideal phase hologram, but in practice it arises from two main factors: ideal phase deviation caused by nonlocal interactions between meta-atoms and variations in their transmittance. Although neural networks have been applied to the design of meta-holograms [42], previous models are typically trained on meta-atom libraries and neglect the influence of nonlocal interactions. In contrast, our method effectively reduces the impact of nonlocal effects, enabling improved hologram performance.

Our optimization strategy is divided into two stages. In the first stage, the diameters of the nanopillars are optimized with their positions fixed at the center of the meta-atoms. In the second stage, the positions of the nanopillars are optimized within a predefined range, but their diameters are fixed according to the previous optimization. The process for each optimization stage follows the flowchart shown in Figure 1a. Here, the conventional design based on the meta-atoms library (neglecting nonlocal interactions) is used to quickly generate an initial structure. And then, our method optimizes this initial structure by manipulating its actual complex amplitude response under nonlocal interactions. To predict the response of meta-atoms under nonlocal interactions, we use a sliding window to decompose the metasurface structure into macrocells [27,28]. The complex amplitude response of the central meta-atom is obtained by simulating a macrocell containing both the central and neighboring meta-atoms (as shown in Figure 1b, crystalline silicon (c-Si) nanopillars on a sapphire substrate are used as meta-atoms). To balance accuracy and efficiency, the macrocell size is set to 9 × 9 meta-atoms (for more details on meta-atom and macrocell design, see Appendix A). This approach allows any metasurface to be decomposed into a series of macrocells, simplifying prediction and optimization via neural networks.

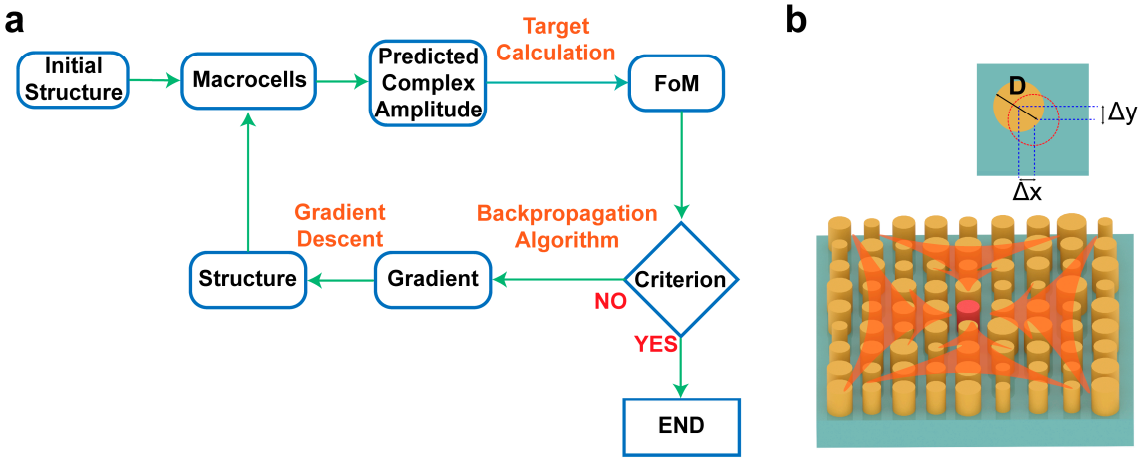

Figure 1. Illustration of the optimization method and the macrocell. (**a**) Illustration of the neural network-based multi-stage gradient optimization method. (**b**) Schematic of the macrocell, where the central meta-atom is influenced by neighboring meta-atoms. Inset, the optimized parameters of a c-Si nanopillar within the meta-atom.

A major design challenge is that each optimization iteration requires simulating millions of macrocells to obtain the complex amplitude of a macroscopic metasurface. Thus, traditional numerical simulation methods, such as the Finite Difference Time Domain

(FDTD) method, become prohibitively time-consuming. Here, we show that PNN is an efficient and practical tool to overcome this challenge. In the first optimization stage, the Prediction Neural Network for Diameter (PNN-D) is used to obtain the complex amplitude of metasurfaces with nanopillars of arbitrary diameters at the center of the meta-atoms. In the second optimization stage, the Prediction Neural Network for Position (PNN-P) is used to obtain the complex amplitude of metasurfaces with nanopillars at arbitrary positions and preset discrete diameters. As shown in Figure 2, for these two networks, 24,000 macrocells were simulated for training and 3000 for testing, by using x-polarized sources. Periodic boundaries were applied, and due to translational symmetry, 81 macrocells were simulated simultaneously in each run, expanding the dataset to 1.94 million instances. Both networks consist of five convolutional layers and four fully connected layers (more details in Appendix B). Implemented in PyTorch (version 1.7.1), the networks used Mean Absolute Error (MAE) as the loss function and the Adaptive Moment Estimation (Adam) optimizer. PNN-D was trained for 30,000 epochs, achieving errors of 0.0887 on the training set and 0.1023 on the test set. PNN-P was trained for 60,000 epochs, with errors of 0.0782 and 0.0791 on the training and test sets, respectively.

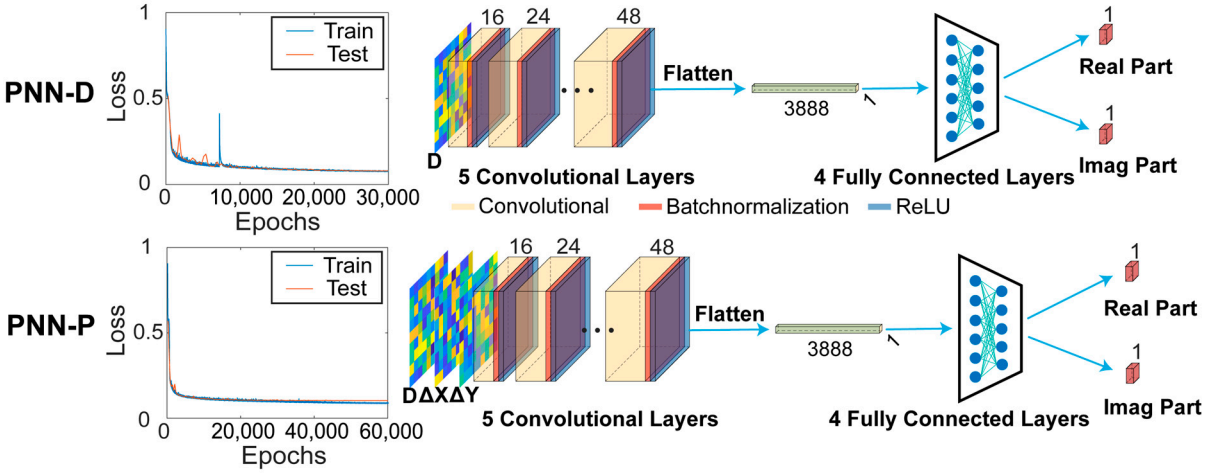

Figure 2. Illustration of network architecture and training process. The loss curves for the training set (blue curve) and test set (red curve) during the training process, along with the network architecture of the PNN-D and PNN-P.

The Figure of Merit (FoM) is then calculated using the predicted complex amplitude distribution and the target complex amplitude distribution of the metasurface structure under x- and y-polarized incident light. The corresponding definitions of the target complex amplitude distribution can be found in Appendix C. The FoM for x- or y-polarized incident light quantifies the difference between the predicted and target complex amplitude distributions, as defined by:

$$\mathrm{FoM_x} = \frac{1}{n}\sum_{i=1}^{n}\left|A_{x,pred,i}\exp(j\varphi_{x,pred,i}) - A_{x,tar,i}\exp(j\varphi_{x,tar,i})\right| \quad (1)$$

$$\mathrm{FoM_y} = \frac{1}{n}\sum_{i=1}^{n}\left|A_{y,pred,i}\exp(j\varphi_{y,pred,i}) - A_{y,tar,i}\exp(j\varphi_{y,tar,i})\right| \quad (2)$$

Here, n represents the number of the meta-atoms, $|\cdot|$ denotes the magnitude of the difference between complex amplitudes, A_{pred} and φ_{pred} correspond to the amplitude and phase of the predicted distribution, and A_{tar} and φ_{tar} correspond to the target distribution. The overall FoM is calculated from the $\mathrm{FoM_x}$ and $\mathrm{FoM_y}$. The smaller the FoM is, the closer

the complex amplitude distribution of the predicted structure is to the target complex amplitude distribution.

$$\mathrm{FoM} = \frac{\sqrt{\mathrm{FoM}_x^2 + \mathrm{FoM}_y^2}}{2} \tag{3}$$

Finally, the gradient optimization is either continued to optimize the structural parameters using the backpropagation algorithm or terminated, depending on whether the number of iterations reaches the preset value or the FoM meets the termination condition. In the backpropagation algorithm, the differentiable pipeline from the optimization parameters to the FoM allows us to calculate the gradient of each nanopillar parameter with respect to the FoM. We then use the Adam optimizer, a gradient descent method, to obtain the optimized structural parameters. Discretization functions (see Appendix D for more details) are then applied to adjust the parameters for subsequent optimization iterations. The parameters of the final optimized structure can thereby meet the discretization requirements.

3. Result

We design and optimize the meta-hologram with a 1000 × 1000 pixel resolution and a structural size of 350 μm × 350 μm, at the operating wavelength of 800 nm. The Fourier holographic phase map is calculated from the target image using the Iterative Fourier transform algorithm [43], and the initial meta-hologram is obtained through the conventional meta-atoms library. It features eight fixed values for the diameter of 500 nm high nanopillars, ranging from 126 nm to 224 nm, arranged in a meta-atom with a 350 nm period (see meta-atom parameters in Appendix A). To simplify experimental fabrication, the final optimized structure retains nanopillars with eight fixed discretized diameters and a 9 nm step size in their positions. The diameters are identical to those used in the phase matching method, while ensuring a minimum interval of more than 50 nm between nanopillars. Considering these factors, the optimization of the diameter D ranges from 100 nm to 240 nm, and the position parameters Δx and Δy range from −36 nm to +36 nm.

Due to the difficulty of simulating the large-scale metasurfaces, we use the prediction results from the PNN-P to obtain the complex amplitude of the metasurfaces. Then, we apply the Fast Fourier Transform (FFT) to simulate the hologram intensity distribution in the k-space. In Appendix E, we verify on a smaller meta-hologram with a size of 87.5 μm × 87.5 μm that the prediction results from the PNN-P closely match the simulation results from the FDTD method from Ansys, Inc. Furthermore, as shown in Appendix E, due to nonlocal interactions between meta-atoms and variations in their transmittance, the complex amplitude distribution of the ideal phase hologram without zero-order energy differs significantly from the simulated results of the original metasurfaces. In our method, we directly optimize the structure by fine-tuning the meta-atoms with the explicit goal of suppressing the zero-order energy. The optimization of the structural parameters may significantly affect the internal modes of the nanopillars and the nonlocal interactions between them (more details in Appendix I). As a result, the complex amplitude distribution of the optimized structure more closely resembles that of the original metasurface rather than the ideal hologram, while still achieving effective zero-order suppression.

The simulation of the initial structure reveals a prominent zero-order component in k-space, significantly brighter than the image area, as shown in Figure 3a. Then, the neural network-based multi-stage gradient optimization is performed (Figure 3b). The two optimization stages are terminated upon completing the 600 iterations for optimizing the diameter and position, and the FoM reaches 6.6×10^{-4}. Comparison between the intensity distribution in the k-space of the optimized structure and that of the original reveals that the zero-order component is significantly reduced, as shown in Figure 3c. The proportion of

zero-order energy decreases to 26% of its original value (Figure 3d), effectively improving the imaging quality by minimizing the zero-order energy.

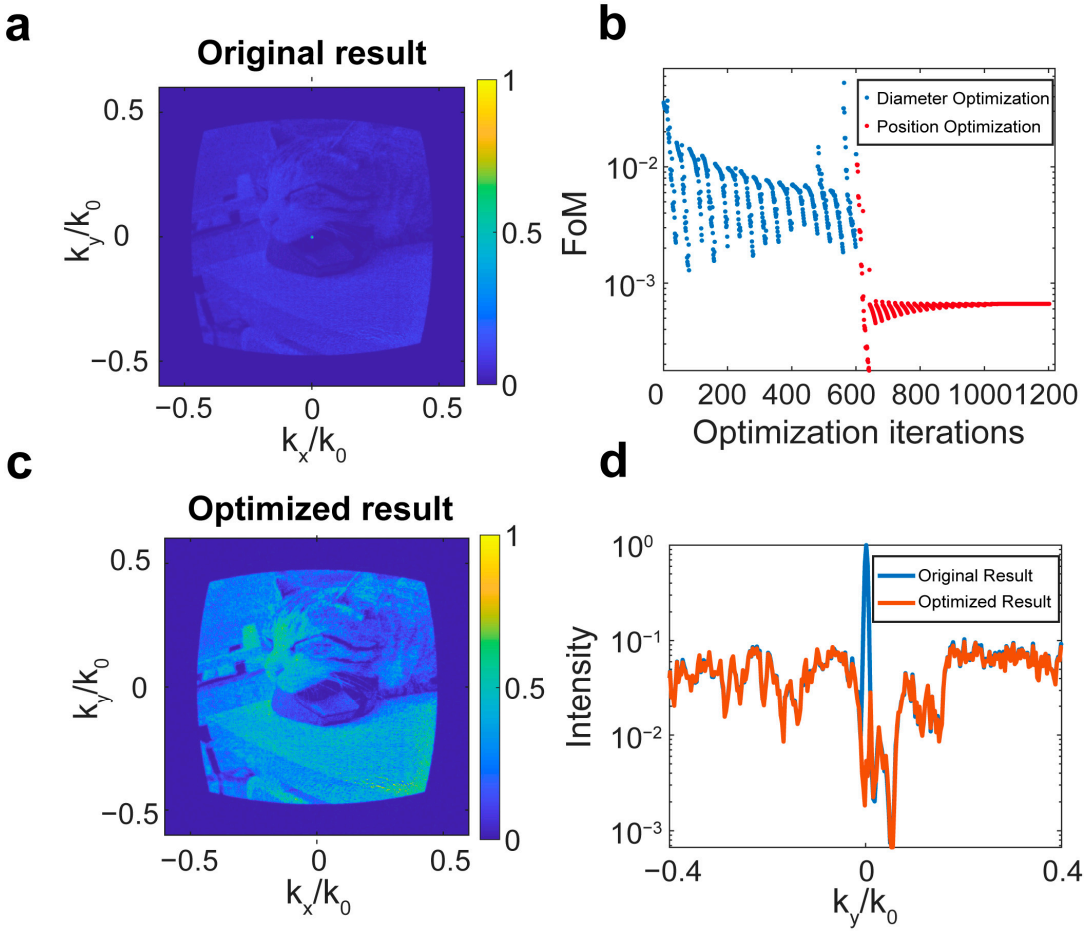

Figure 3. Optimization results of the meta-holograms. (**a**) Simulated hologram intensity distribution of the metasurface structure using the phase matching method in the k-space. (**b**) FoM during the optimization process with eight fixed values for the nanopillar diameter and a 9 nm step size for the nanopillar positions. The iterations for diameter optimization are shown as blue dots, and the iterations of position optimization are shown as red dots. (**c**) Simulated hologram intensity distribution of the optimized metasurface structure in the k-space. (**d**) Hologram intensity distribution along $k_x = 0$ in the (**a**,**c**). Inset shows the ideal reconstructed image of the meta-holograms.

By using this method, many meta-atoms and complex wavefront distributions can be designed with relatively little computational time, even less than the simulation time required for the entire metasurface in FDTD (more details in Appendix F). It is worth noting that, during the optimization process, if the position step size is changed to a stricter requirement of 1 nm for fabrication, then the obtained optimization results are similar, as shown in Appendix G.

SEM (Zeiss Auriga) micrographs of the structure of size 350 μm × 350 μm and fabricated using electron beam lithography are shown in Figure 4a. To minimize the impact of incident light outside the structure, a square aperture diaphragm of 350 μm is used, aligned and fixed with the metasurface.

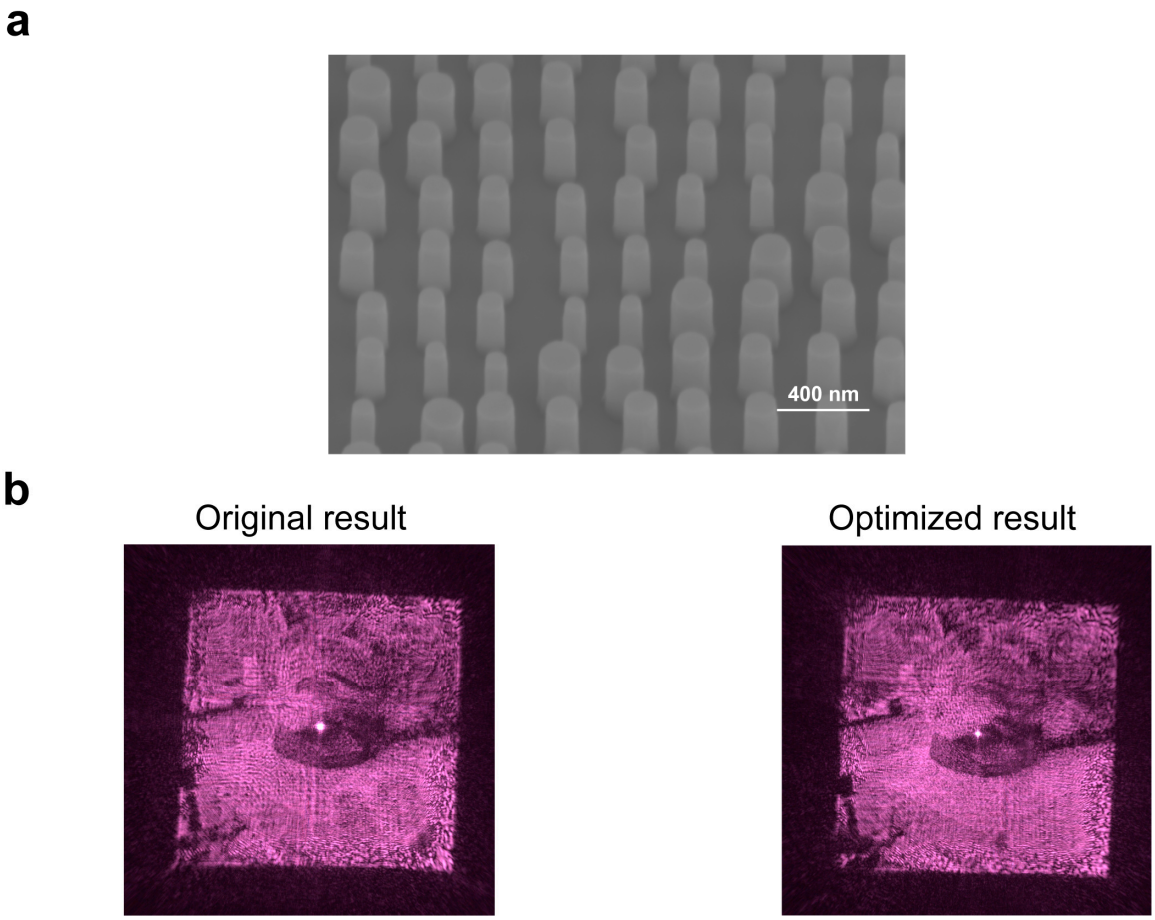

Figure 4. Experimental results of the meta-holograms. (**a**) The SEM of the metasurface structure. (**b**) The captured hologram intensity distribution before and after optimization under 800 nm incident light.

The imaging optical setup is used to capture the hologram intensity distribution of the meta-holograms with an 800 nm laser light source. The power of the zero-order light is obtained by measuring the intensity within a circle of diameter 3 × FWHM of the zero-order light in the CMOS imaging plane. The proportion of zero-order energy after optimization is reduced to 57% of its initial value in the experiment (more details in Appendix H), compared to 26% in the simulation. This discrepancy is mainly attributed to fabrication errors, which are not accounted for in the optimization process. Specifically, deviations in the diameters of the nanopillars have a significant influence on the zero-order component, as shown in Appendix J. As shown in Figure 4b, the zero-order over-exposure area in the hologram intensity distribution of the original structure is significantly larger than in the optimized structure, thus leading to a more pronounced impact on the image quality.

4. Discussion and Conclusions

In conclusion, we propose a neural network-based multi-stage gradient optimization method that takes the ideal performance of the metasurface as the optimization target. This approach enables efficient modulation of nonlocal interactions, thereby significantly enhancing the overall performance of the metasurface. This multi-stage optimization strategy, using multiple network models, resolves the trade-off between gradient calculation accuracy and the number of optimized parameters. Additionally, discretization ensures that the optimized parameters meet preset fabrication requirements. Together, these features provide a practical and fast approach for optimizing large-scale metasurfaces.

Through simulations and experiments, we applied this method to suppress the zero-order component of meta-holograms by optimizing the complex amplitude of the meta-atoms considering nonlocal interactions. We showed a theoretical zero-order energy reduction to 26% of its original value, and the intensity dropped to the same level as the image area. Experimentally, the zero-order energy was reduced to 57%. To reduce the discrepancy between the experimental and theoretical results, the method's robustness can be enhanced by incorporating error-aware training or robustness strategies [19]. This approach may reduce the impact of fabrication errors on the optimized structure, making the optimization method more practical for real-world applications. Unlike other methods [5,34,36], our approach adjusts the diameters and positions of nanopillars within the meta-atoms, without additional optical components or restrictions on phase units. This makes ours a versatile method to control nonlocal interactions, enabling efficient applications of metasurfaces with intricate complex-amplitude designs. To further test the generality of our method, we used it to optimize a beam deflector and improve its deflection efficiency (more details in Appendix I). By extending the network to predict the complex amplitudes for multiple wavelengths and different polarization components, our method can be applied to the regulation of complex polarization distributions and broad-spectrum responses in imaging, sensing, and communication, like polarization converters or achromatic metalenses. Moreover, by integrating it with differentiable computational processes, like diffraction calculations [31], more applications with complex light field distributions can be realized, like multi-focus [44] or multi-topological beam focusing [45].

Author Contributions: H.L. and J.L. conceived the idea of the paper; Y.Z. performed the calculations; Y.Z. and Q.X. finished the experiment; Y.Z., Y.L., E.R.M., H.L. and J.L. wrote the manuscript. All authors contributed to the analysis of the results. All authors have read and agreed to the published version of the manuscript.

Funding: This work was funded by the National Key R&D Program of China (No. 2022YFA1404304), National Natural Science Foundation of China (Nos. 12374363, 12074444, and 11704421), Guangdong Basic and Applied Basic Research Foundation (No. 2020B0301030009). H.L. acknowledges the "GDTZ" plan support under contract No. 2021TQ06X161. J.L. and H.L. are supported by Guangdong Provincial Quantum Science Strategic Initiative) (GDZX2306002) and Guangdong Provincial Natural Science Fund Projects (2024B1515040013). E.R.M. acknowledges funding from Fapesp (grant #00619-4) and CNPq (grant 307602/2021-4).

Institutional Review Board Statement: Not applicable.

Informed Consent Statement: Not applicable.

Data Availability Statement: The data are contained within the article.

Conflicts of Interest: The authors declare no conflicts of interest.

Appendix A. The Design of Meta-Atoms and Macrocell

We construct a meta-atoms library consisting of 500 nm high c-Si nanopillars on a sapphire substrate, arranged with a 350 nm period for an 800 nm incident light, as shown in Figure A1. The sapphire substrate has a refractive index of 1.76 (and no absorption), while crystalline silicon has a refractive index of 3.69 and an extinction coefficient of 0.006. We note that crystalline silicon on sapphire has been used for full-color imaging in the visible range with high performance [46]. We simulate meta-atoms with different diameters in Ansys FDTD, setting periodic boundary conditions and an x-polarized plane incident source. Eight nanopillars with diameters ranging from 126 nm to 224 nm are selected, and the lowest transmittance among the selected nanopillars exceeds 80%, as detailed in Table A1.

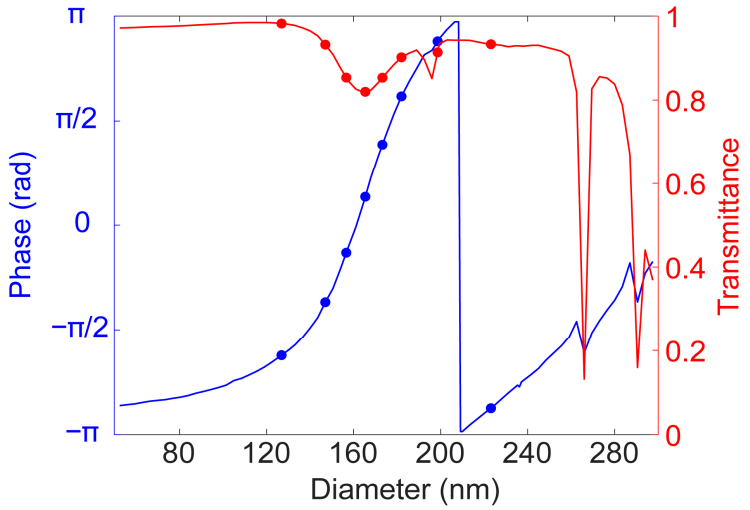

Figure A1. The phase (blue dots) and transmittance (red dots) of the selected eight nanopillars, along with the phase (blue line) and transmittance (red line) of the meta-atoms library under periodic boundary conditions.

Table A1. Transmittance and phase of the eight selected nanopillars.

Diameter (nm)	126	146	156	166	174	182	198	224
Phase (rad)	$-5\pi/8$	$-3\pi/8$	$-\pi/8$	$\pi/8$	$3\pi/8$	$5\pi/8$	$7\pi/8$	$-7\pi/8$
Transmittance	0.98	0.93	0.85	0.82	0.85	0.90	0.91	0.93

For the macrocell, a point monitor is positioned 200 nm above the structure to record the complex amplitude response of the central meta-atom. Meta-atoms outside the macrocell area have minimal influence on the central meta-atom; hence, periodic boundary conditions are applied in the macrocell simulation. During the decomposition of the metasurface into macrocells, the metasurface is treated as a periodic structure, allowing empty regions of the macrocells at the edges of the metasurface to be filled with meta-atoms from the adjacent period.

Appendix B. Neural Network Architecture

The neural networks, PNN-D and PNN-P, feature a structure consisting of five convolutional layers (Conv) followed by four fully connected layers (FC). This architecture is designed to predict the real and imaginary components of the complex amplitude response. To enhance the generalization ability of the networks, we employ batch normalization layers and dropout layers. However, the inputs of these networks are different. For PNN-D, since only the diameter of the nanopillar is used as input, the size of the input tensor is $9 \times 9 \times 1$; in PNN-P, however, both the diameter and position of the nanopillar are used as inputs. Therefore, the size of the input tensor is expanded to $9 \times 9 \times 3$. Detailed parameters are provided in Figure A2.

PNN-D		PNN-P	
Layer	Kernel size and other setting	Layer	Kernel size and other setting
Conv_2d_1	3×3×1×16, stride = 1, padding = 1	Conv_2d_1	3×3×3×16, stride = 1, padding = 1
Batchnorm_2d, ReLU		Batchnorm_2d, ReLU	
Conv_2d_2	3×3×16×24, stride = 1, padding = 1	Conv_2d_2	3×3×16×24, stride = 1, padding = 1
Batchnorm_2d, ReLU		Batchnorm_2d, ReLU	
Conv_2d_3	3×3×24×32, stride = 1, padding = 1	Conv_2d_3	3×3×24×32, stride = 1, padding = 1
Batchnorm_2d, ReLU		Batchnorm_2d, ReLU	
Conv_2d_4	3×3×32×40, stride = 1, padding = 1	Conv_2d_4	3×3×32×40, stride = 1, padding = 1
Batchnorm_2d, ReLU		Batchnorm_2d, ReLU	
Conv_2d_5	3×3×40×48, stride = 1, padding = 1	Conv_2d_5	3×3×40×48, stride = 1, padding = 1
Batchnorm_2d, ReLU		Batchnorm_2d, ReLU	
Flatten		Flatten	
FC_1	3888×1024	FC_1	3888×1024
Batchnorm_1d, ReLU, Dropout (0.1)		Batchnorm_1d, ReLU, Dropout (0.1)	
FC_2	1024×512	FC_2	1024×512
Batchnorm_1d, ReLU, Dropout (0.1)		Batchnorm_1d, ReLU, Dropout (0.1)	
FC_3	512×256	FC_3	512×256
Batchnorm_1d, ReLU, Dropout (0.1)		Batchnorm_1d, ReLU, Dropout (0.1)	
FC_4	256×2	FC_4	256×2

Figure A2. The neural network architecture for PNN-D and PNN-P.

Appendix C. The Definition of the Target Complex Amplitude Distribution

For x-polarized incident light, the complex amplitude is directly predicted by the networks. For y-polarized incident light, the macrocell is first rotated by 90 degrees before prediction, as shown in Figure A3. As shown in Figure A4, after applying the Fast Fourier Transform (FFT), the spatial spectrum amplitude distribution in the k-space is modified by replacing the image area with the meta-hologram image from the initial structure but without the zero-order component, constructing the desired spatial spectrum amplitude distribution. The Inverse Fast Fourier Transform (IFFT) is then used to calculate and update the target complex amplitude distribution in each iteration.

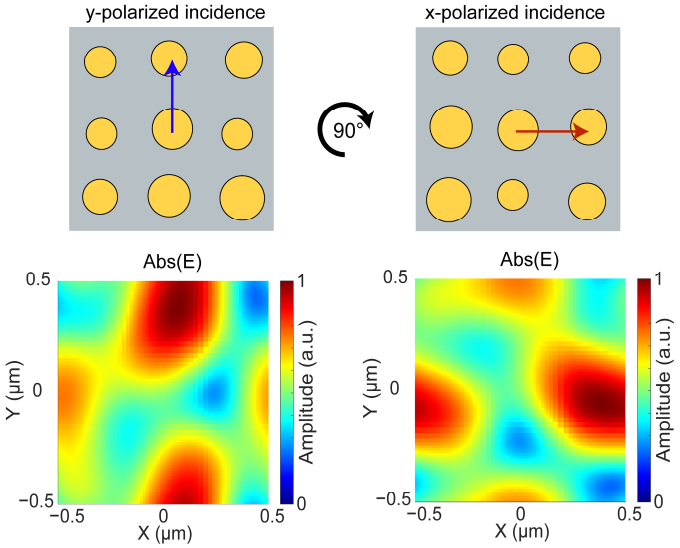

Figure A3. The simulation result of the structure under y-polarized incidence (**left**), and that of the structure rotated by 90° under x-polarized incidence (**right**).

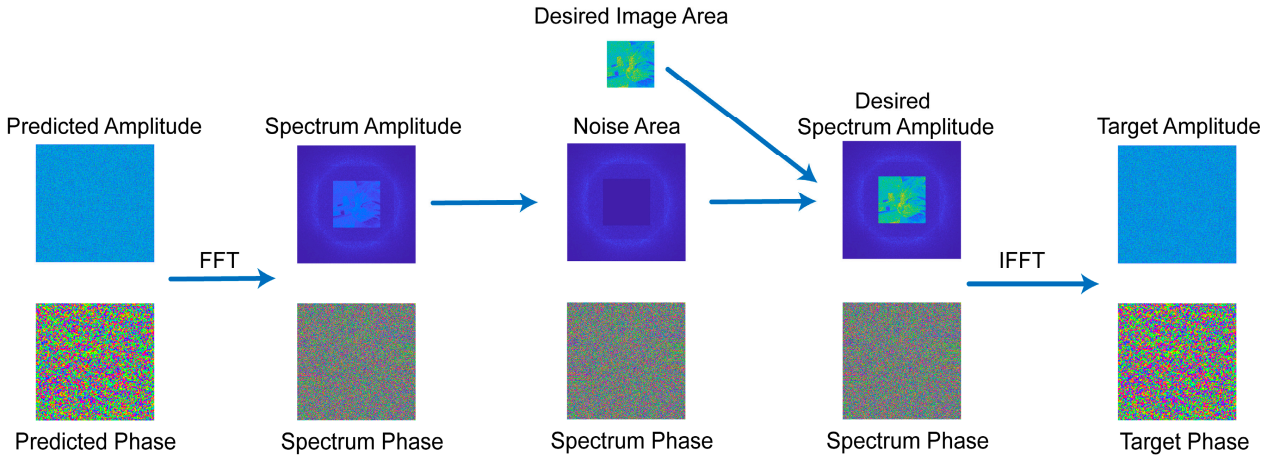

Figure A4. Flowchart illustrating the target complex amplitude calculation process.

Appendix D. The Definition of Discretization Functions

To achieve a final optimized structure retaining nanopillars with eight fixed discretized diameters, identical to those used in the phase matching method, we design discretization functions based on the sigmoid function. The eight fixed discretized diameters are normalized to the range [0, 1] using min–max normalization within the optimization range of 100 nm to 240 nm, as shown in Table A2. For the n-th iteration in the diameter optimization stage, the discretization function is defined as:

$$D(d) = \begin{cases} d & \mathrm{mod}(n, 40) \neq 0 \\ b_1 - \frac{a_1}{2} + \sum_{i=1}^{k-1} \frac{a_i}{1 + \exp[-\beta_d (d - b_i)/a_i]} & \mathrm{mod}(n, 40) = 0 \end{cases}, \quad \text{(A1)}$$

where mod(·) means the remainder, d is the set of the optimized diameters of the nanopillars after applying the gradient descent method, D is the set of diameters for subsequent optimization iterations, k represents the number of preset discrete diameters, β_d represents the binary coefficient, and a_i and b_i are the difference and the average of two adjacent normalized diameters (Table A2). Here, β_d increases gradually during the optimization process to ensure convergence of the optimized diameters to discrete values.

$$\beta_d = 10 \times 1.5^{\lfloor n/40 \rfloor}, \quad \text{(A2)}$$

where $\lfloor\ \rfloor$ means rounding downwards.

Table A2. Preset discrete values for diameter optimization.

Diameter (nm)	126	146	156	166	174	182	198	224
Normalized diameter	0.186	0.329	0.400	0.471	0.529	0.586	0.700	0.886
a_i	0.143	0.071	0.071	0.057	0.057	0.114	0.186	
b_i	0.257	0.364	0.436	0.500	0.557	0.643	0.793	

Similarly, the nanopillar positions are normalized to the range $[-1, 1]$ using min–max normalization within the optimization range of -36 nm to 36 nm, as shown in Table A3. For the n-th iteration in position optimization stage, the discretization function is defined as:

$$\Delta X(\Delta x) = \begin{cases} \Delta x & \mathrm{mod}(n, 20) \neq 0 \\ f_1 - \frac{e_1}{2} + \sum_{i=1}^{j-1} \frac{f_i}{1 + \exp[-\beta_p(\Delta x - f_i)/e_i]} & \mathrm{mod}(n, 20) = 0' \end{cases} \quad \text{(A3)}$$

$$\Delta Y(\Delta y) = \begin{cases} \Delta y & \mathrm{mod}(n, 20) \neq 0 \\ f_1 - \frac{e_1}{2} + \sum_{i=1}^{j-1} \frac{f_i}{1 + \exp[-\beta_p(\Delta y - f_i)/e_i]} & \mathrm{mod}(n, 20) = 0 \end{cases} \quad \text{(A4)}$$

where Δx and Δy are the optimized positions of the nanopillars after applying the gradient descent method, ΔX and ΔY are the sets of positions for subsequent optimization iterations, j represents the number of preset discrete positions, β_p is the binary coefficient, set as 10×1.5^{15}, and e_i and f_i represent the difference and the average of two adjacent normalized positions, as shown in Table A3.

Table A3. Preset discrete values for position optimization.

Position (nm)	−36	−27	−18	−9	0	9	18	27	36
Normalized position	−1	−0.75	−0.5	−0.25	0	0.25	0.5	0.75	1
e_i	0.25	0.25	0.25	0.25	0.25	0.25	0.25	0.25	
f_i	−0.875	−0.625	−0.375	−0.125	0.125	0.375	0.625	0.875	

Appendix E. Prediction Results Compared with Simulation Results

We design and optimize a meta-hologram with a resolution of 250 × 250 pixels and a structural size of 87.5 μm × 87.5 μm. The optimization process and settings are the same as those used for the 350 μm × 350 μm metasurfaces described in the main text. The final FoM is 7.42×10^{-4}. We use the PNN-P to predict and FDTD to simulate the complex amplitude of the metasurfaces. In FDTD, we set the Perfectly Matched Layer (PML) boundary conditions and a 45° linearly polarized plane source, as shown in Figure A7. Then, we apply FFT to simulate the corresponding hologram intensity distribution. As shown in Figure A5, the results from both methods are similar. What is more, as shown in Figure A8, with the same maximum intensity scale, the hologram intensity distribution of the original structure is similar to that of the optimized structure, except for the zero-order component.

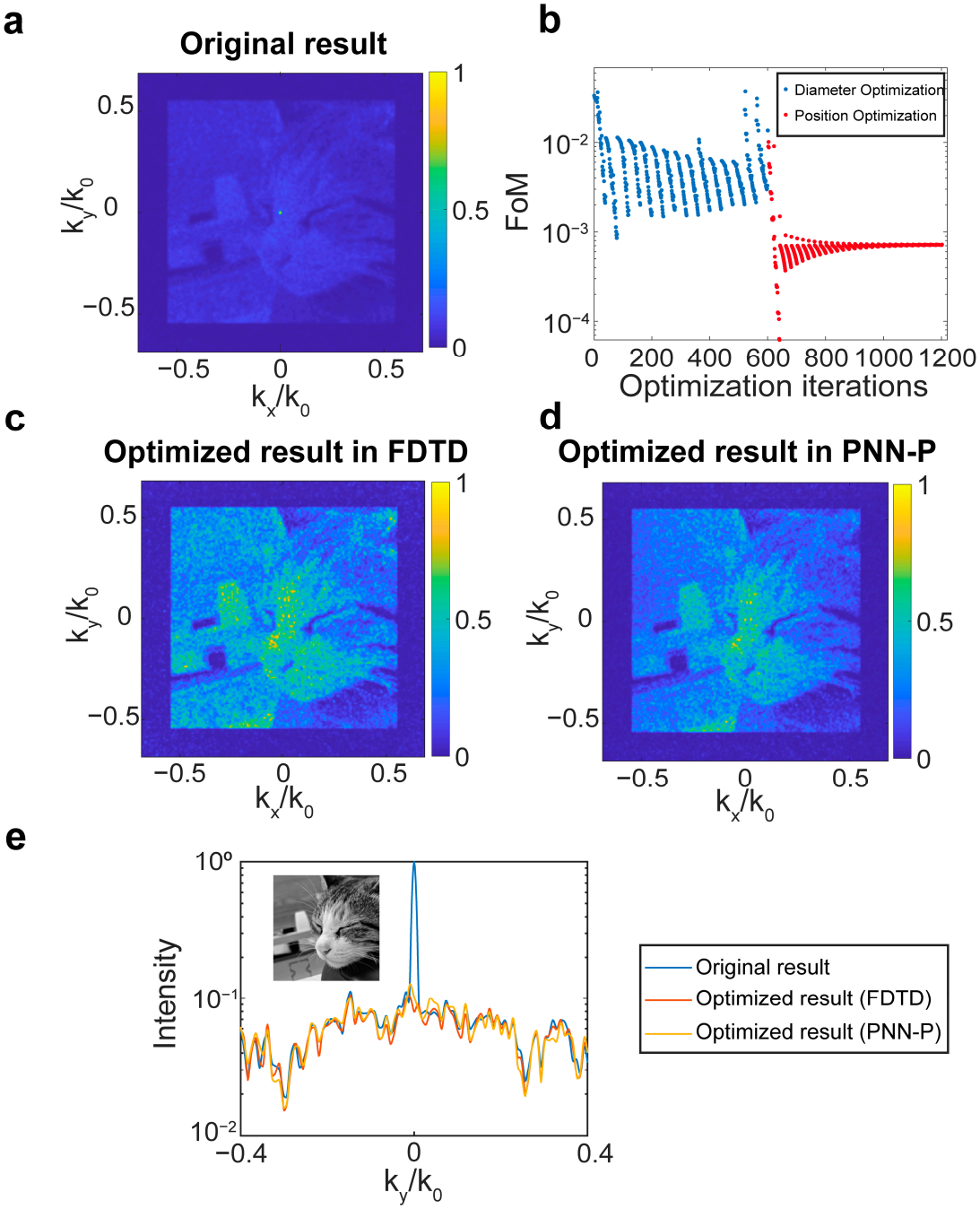

Figure A5. Optimization results of the meta-holograms. (**a**) Simulated hologram intensity distribution of the metasurface structure using the phase matching method in the k-space by FDTD and FFT. (**b**) FoM during the optimization process with eight fixed values for the nanopillar diameter and a 9 nm step size for the nanopillar positions. The iterations for diameter optimization are shown as blue dots, and the iterations of position optimization are shown as red dots. (**c**) Simulated hologram intensity distribution of the optimized metasurface structure in the k-space by FDTD and FFT. (**d**) Predicted hologram intensity distribution of the optimized metasurface structure in the k-space by PNN-P and FFT. (**e**) Hologram intensity distribution along $k_x = 0$ in the (**a**,**c**,**d**). Inset shows the ideal reconstructed image of the meta-holograms.

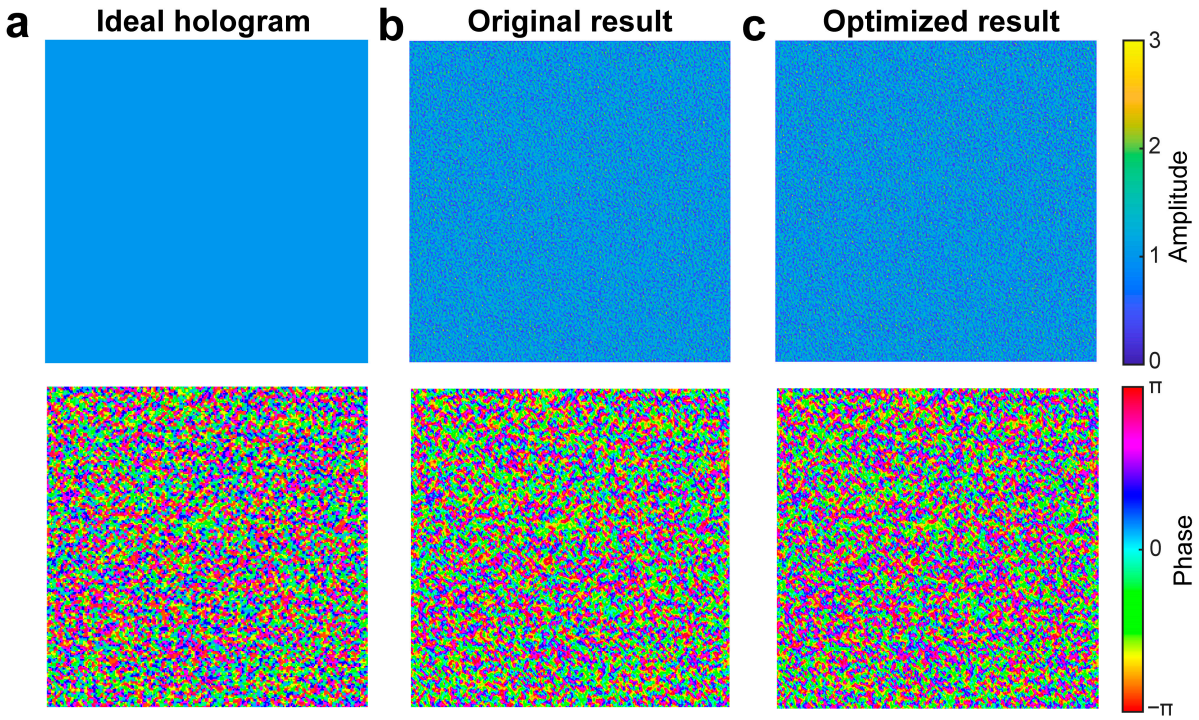

Figure A6. The complex amplitude distribution of different results. (**a**) Ideal phase hologram. (**b**) Original structure in FDTD. (**c**) Optimized structure in FDTD.

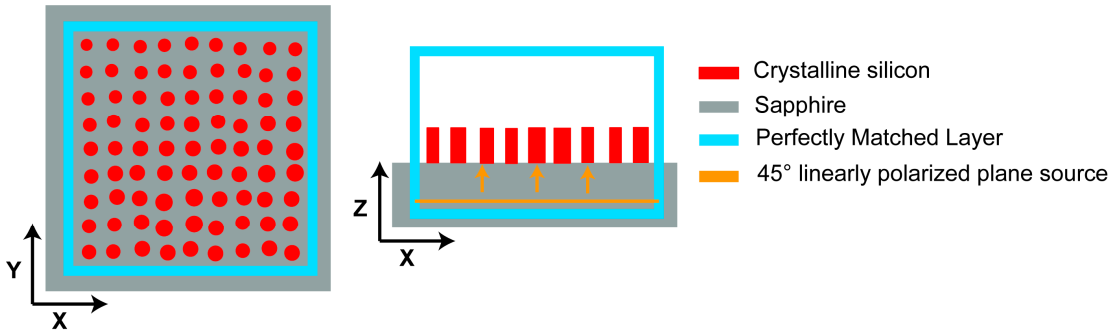

Figure A7. The illustration of the simulation settings.

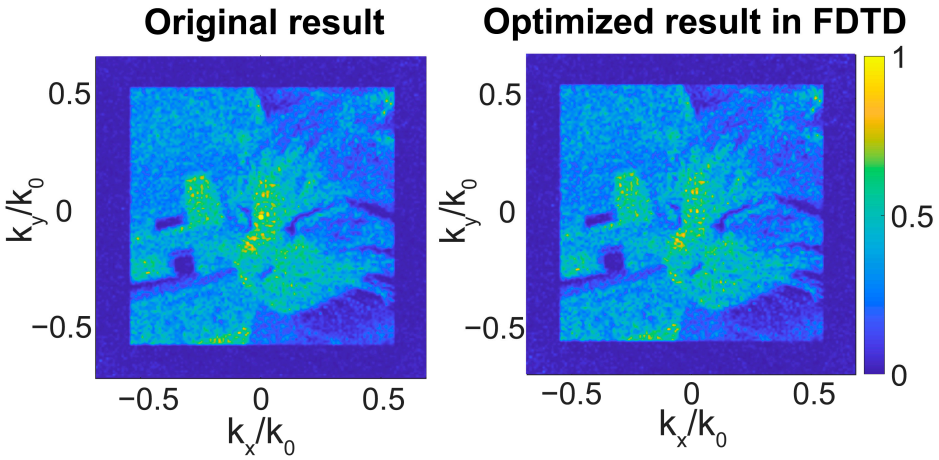

Figure A8. Simulated hologram intensity distributions of the original and the optimized metasurface structures in the k-space by FDTD and FFT with the same maximum intensity scale.

Appendix F. Calculation Time Efficiency

We collect the dataset on a dual-CPU server equipped with two 28-core Intel Xeon Platinum 8176 processors from Intel, Santa Clara, CA, USA, over nearly 20 days. The neural network models are trained on a GPU server equipped with an NVIDIA RTX 3080Ti,, from NVIDIA, Santa Clara, CA, USA, with each model requiring approximately 8 h for training. Optimization of two meta-holograms with different sizes is performed on the GPU server, while FDTD simulations for the final optimized structures are executed on the CPU server. However, due to the significant computational resource demands and challenges in loading the largest structure into the simulation environment, the large structure could not be simulated via FDTD on our server. The times spent on optimization and simulation for each structure are listed in Table A4.

Table A4. Optimization and simulation times for optimized meta-hologram structures of different sizes.

Structure Size (μm × μm)	Number of Pixels	Optimization Time (mins)	Simulation Time (mins)
87.5 × 87.5	250 × 250	52	600
350 × 350	1000 × 1000	227	---

Appendix G. Optimization with Eight Fixed Values for the Nanopillar Diameter and a 1 nm Step Size for the Nanopillar Positions

As shown in Figure A9, reducing the step size from 9 nm (Figure A5) to 1 nm does not significantly affect the optimization results. The intensity of the zero-order component becomes nearly identical to that of the image area, with noise making it indistinguishable. The FoM corresponding to the 1 nm step size was approximately 9.46×10^{-5}. The results indicate that although a smaller FoM means better optimization results, the effect of zero-order suppression is already sufficient when the FoM is ~10^{-4}.

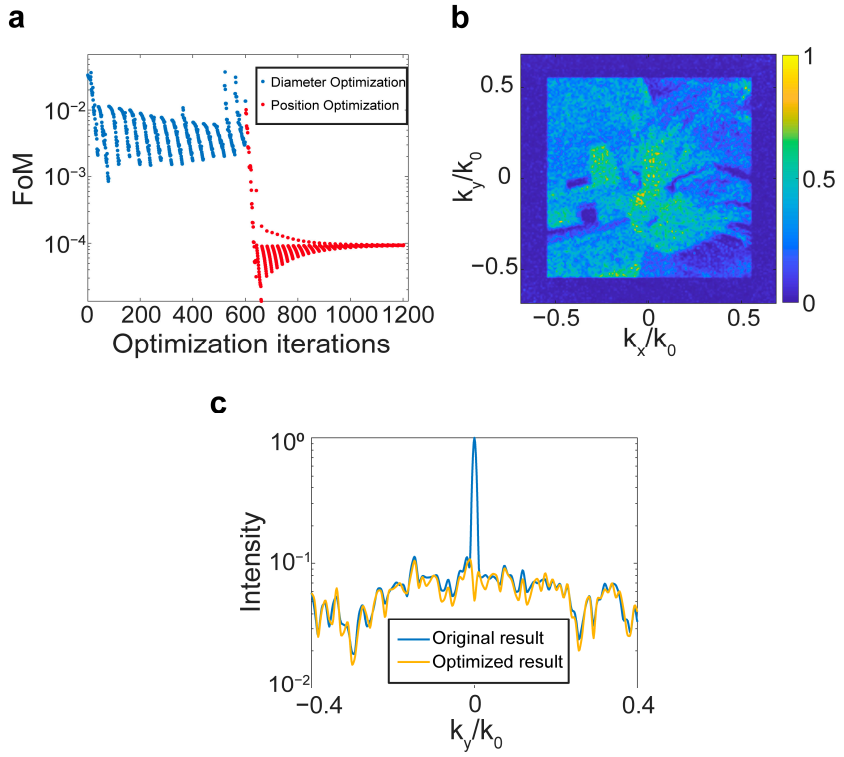

Figure A9. Optimization result of the meta-hologram with size of 87.5 μm. (**a**) FoM during the optimization process with eight fixed values for the nanopillar diameter and a 1 nm step size for the

nanopillar positions. The iterations for diameter optimization are shown as blue dots, and the iterations of position optimization are shown as red dots. (**b**) Simulated hologram intensity distribution of the optimized metasurfaces structure in the k-space. (**c**) Hologram intensity distribution along $k_x = 0$ in the (**b**) and Figure A5a.

Appendix H. The Fabrication Process and the Optical Measurement

The sample is fabricated on a commercially available Silicon on Sapphire (SOS) wafer with a 500 nm thick c-Si film. A 220 nm thick hydrogen silsequioxane (HSQ) electron beam resist is spin-coated onto the film, followed by a 30 nm thick aluminum layer deposited using a thermal evaporator. Electron beam lithography (Raith Vistec EBPG 5000+, from Raith, Dortmund, Germany) is used to define the structure. After removing the aluminum mask and developing the resist, inductively coupled plasma etching (PlasmaPro System 100 ICP180, from Oxford Instruments, Oxford, UK) transfers the pattern from the resist to the silicon layer. Finally, the remaining HSQ resist is removed using hydrofluoric acid.

The imaging optical setup, shown in Figure A10, includes an 800 nm laser for incident light and a CMOS (Kiralux CS895CU, from Throlabs, Newton, NJ, USA) from Thorlabs to capture the image. In both the original structure and the optimized structure, the CMOS images do not exhibit overexposure, and the exposure settings are the same, as shown in Figure A11.

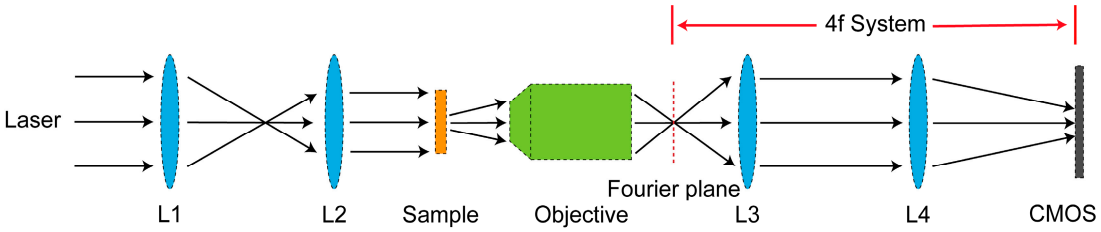

Figure A10. Schematic of the optical setups for capturing the reconstructed image.

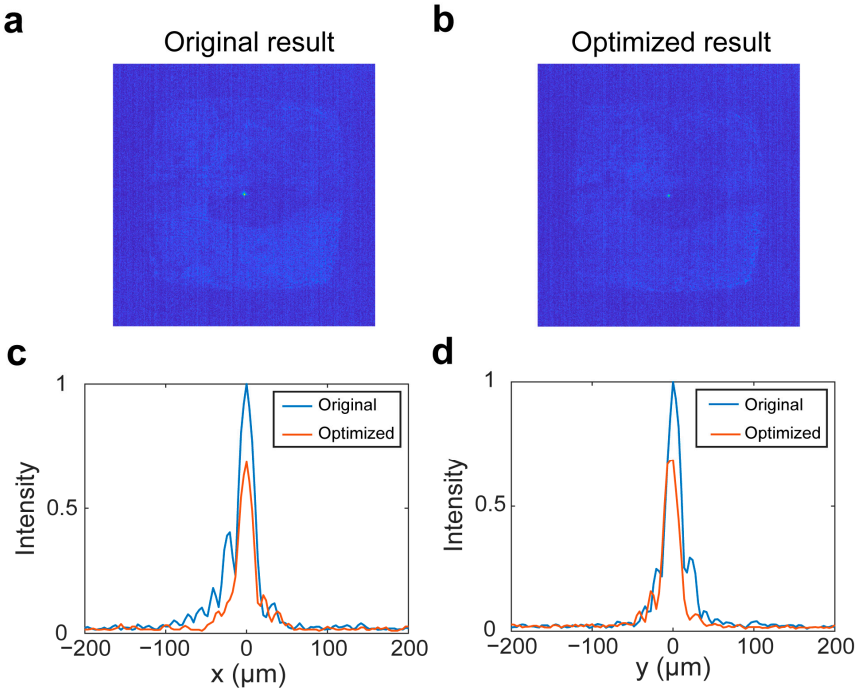

Figure A11. The experimental results of the meta-holograms without overexposure. The captured hologram intensity distribution of the (**a**) original structure and (**b**) optimized structure on a logarithmic scale. The hologram intensity distribution along (**c**) the horizontal and (**d**) vertical direction.

Appendix I. Optimization of Beam Deflector and Nonlocal Interactions

To further test the generality of our optimization method, we optimize a beam deflector composed of four nanopillars. Through the phase matching method, we select four appropriate nanopillars from Table A1 as the original structure. We optimize the diameters of the nanopillars and ignore the discretization constraints. The optimization objective is to maximize the +1st order intensity of the complex amplitude distribution of the deflector predicted by the network, PNN-D. The diameters of the nanopillars before and after optimization are shown in Table A5. The original and the optimized deflectors are simulated in FDTD, with periodic boundary conditions and an x-polarized plane incident source set up. The phase distribution of the Ex component on the xz plane and the far-field intensity distribution are shown in Figure A12. The optimized beam deflector features a smoother wavefront, which means higher deflection efficiency, increasing from 33.1% to 68.4%. The electric field amplitude distributions inside the deflectors before and after optimization are shown in Figures A13a and A13b, respectively. The near-field coupling is manifested as a field distribution overlapping two (or more) nanopillars. For nanopillars with smaller sizes, the electric field distribution outside the nanopillars is more pronounced, which enhances near-field coupling. The effect of optimization can be seen by inspection of the fields in Figure A13a,b: there is less field overlap between adjacent nanopillars in the optimized structure (Figure A13b) than in the non-optimized structure (Figure A13a).

Table A5. The diameters of nanopillars in the original and the optimized beam deflectors.

Diameter (nm)	Original	166	182	224	146
	Optimized	167	188	226	151

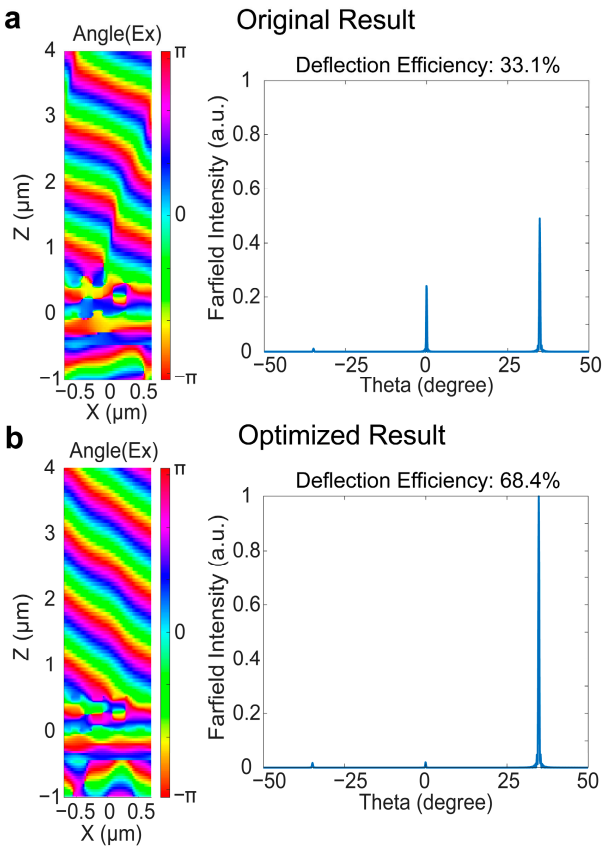

Figure A12. The simulation results of the (**a**) original and the (**b**) optimized beam deflectors. The left side is the phase distribution of the Ex component; the right side is the far-field intensity distribution.

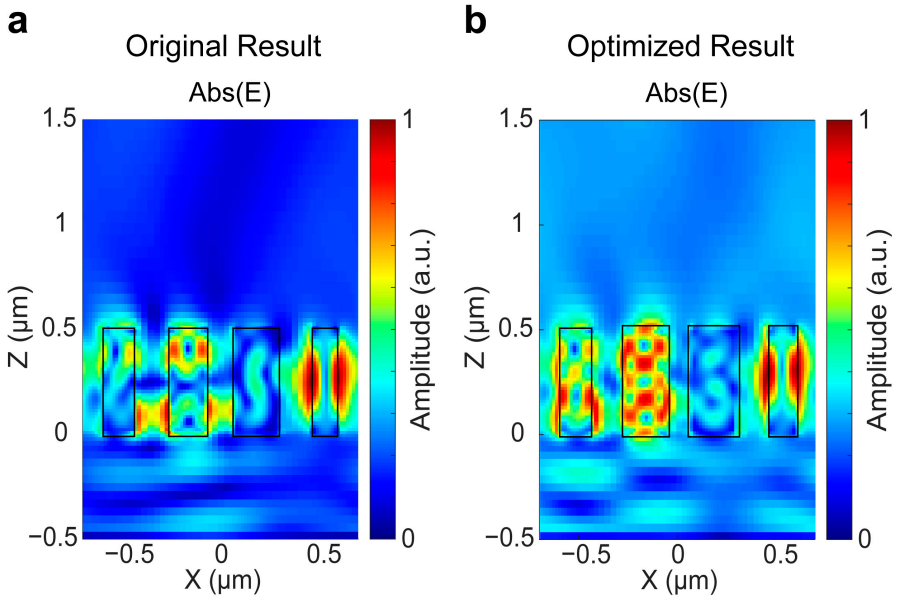

Figure A13. The electric field amplitude distributions of the (**a**) original and the (**b**) optimized beam deflectors in xz plane.

Appendix J. Influence of Diameter Deviations

Based on the optimized structure in Appendix E, we increase or decrease the diameters of all nanopillars by 2 nm to evaluate the influence of diameter deviations on the zero-order component. As shown in Figure A14, the zero-order component of the structure significantly increases from 26% to 64%, which means the optimized structure is sensitive to the deviations of the structural parameters.

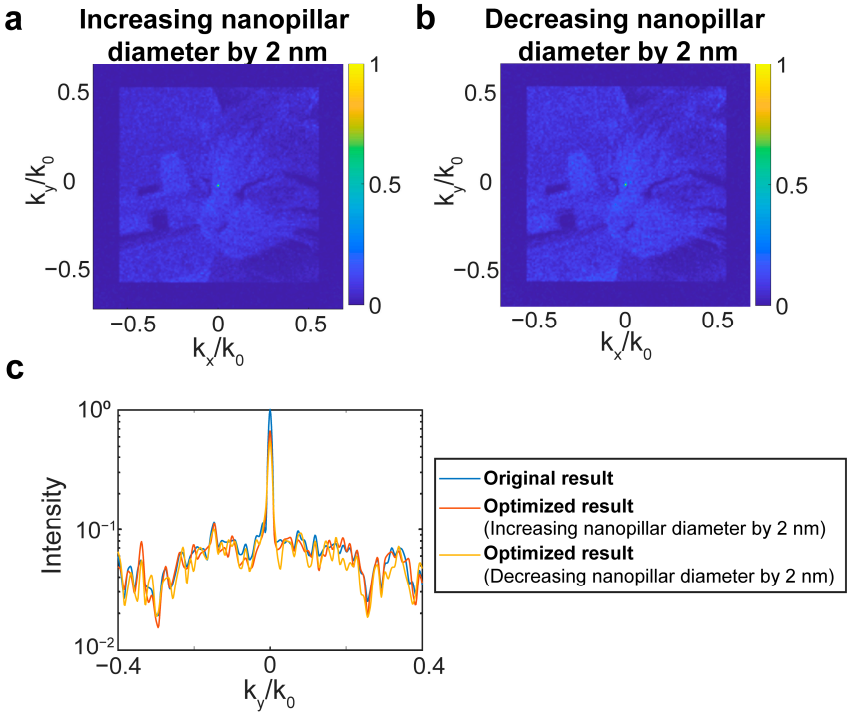

Figure A14. The simulation results of the optimized meta-holograms with diameter deviations. (**a**) Simulated hologram intensity distribution in the k-space of the metasurface structure after increasing the nanopillar diameter by 2 nm. (**b**) Simulated hologram intensity distribution in the k-space of the metasurface structure after decreasing the nanopillar diameter by 2 nm. (**c**) Hologram intensity distribution along $k_x = 0$ in (**a**), (**b**) and Figure A5a.

Appendix K. Influence of Smaller Dataset

We tested the influence of smaller datasets, i.e., 970k and 485k samples, on our network model. As shown in Figure A15, smaller datasets lead to overfitting, which means that the network performs well on the training dataset but poorly on the new data from the test dataset.

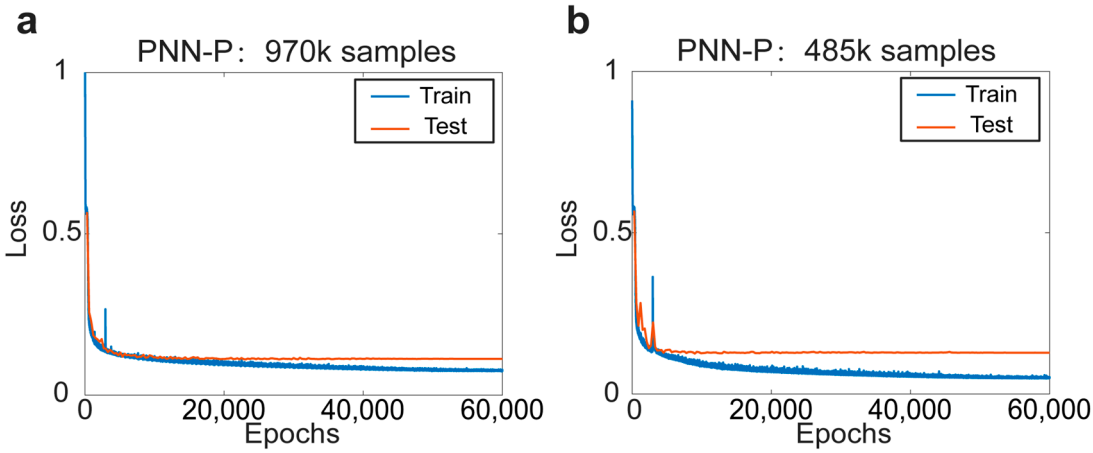

Figure A15. The loss curves for the training set (blue curve) and test set (red curve) during the training process for different datasets, (**a**) 970k samples and (**b**) 485k samples.

References

1. Chen, J.; Ye, X.; Gao, S.; Chen, Y.; Zhao, Y.; Huang, C.; Qiu, K.; Zhu, S.; Li, T. Planar wide-angle-imaging camera enabled by metalens array. *Optica* **2022**, *9*, 431–437. [CrossRef]
2. Chen, W.T.; Zhu, A.Y.; Sanjeev, V.; Khorasaninejad, M.; Shi, Z.; Lee, E.; Capasso, F. A broadband achromatic metalens for focusing and imaging in the visible. *Nat. Nanotechnol.* **2018**, *13*, 220–226. [CrossRef]
3. Chang, S.; Zhang, L.; Duan, Y.; Rahman, M.T.; Islam, A.; Ni, X. Achromatic metalenses for full visible spectrum with extended group delay control via dispersion-matched layers. *Nat. Commun.* **2024**, *15*, 9627. [CrossRef]
4. You, X.; Ako, R.T.; Sriram, S.; Withayachumnankul, W. 3D Terahertz Confocal Imaging with Chromatic Metasurface. *Laser Photonics Rev.* **2025**, *19*, 2401011. [CrossRef]
5. Zheng, G.; Mühlenbernd, H.; Kenney, M.; Li, G.; Zentgraf, T.; Zhang, S. Metasurface holograms reaching 80% efficiency. *Nat. Nanotechnol.* **2015**, *10*, 308–312. [CrossRef] [PubMed]
6. Wang, D.; Li, Y.; Zheng, X.; Ji, R.; Xie, X.; Song, K.; Lin, F.; Li, N.; Jiang, Z.; Liu, C.; et al. Decimeter-depth and polarization addressable color 3D meta-holography. *Nat. Commun.* **2024**, *15*, 8242. [CrossRef] [PubMed]
7. Yang, H.; Peng, M.; He, H.; Yu, D.; Ou, K.; Wang, Q.; Luo, X.; Hu, Y.; Jing, H.; Duan, H. Polarization-Independent Dispersive Complex-Amplitude Modulation via Anisotropic Metasurfaces. *Laser Photonics Rev.* **2025**, *19*, 2401398. [CrossRef]
8. Deng, M.; Kanwal, S.; Wang, Z.; Cai, C.; Cheng, Y.; Guan, J.; Hu, G.; Wang, J.; Wen, J.; Chen, L. Dielectric Metasurfaces for Broadband Phase-Contrast Relief-Like Imaging. *Nano Lett.* **2024**, *24*, 14641–14647. [CrossRef]
9. He, H.; Zhang, Y.; Shao, Y.; Zhang, Y.; Geng, G.; Li, J.; Li, X.; Wang, Y.; Bian, L.; Zhang, J.; et al. Meta-Attention Network Based Spectral Reconstruction with Snapshot Near-Infrared Metasurface. *Adv. Mater.* **2024**, *36*, 2313357. [CrossRef]
10. Zhou, Z.; Li, J.; Su, R.; Yao, B.; Fang, H.; Li, K.; Zhou, L.; Liu, J.; Stellinga, D.; Reardon, C.P.; et al. Efficient Silicon Metasurfaces for Visible Light. *ACS Photonics* **2017**, *4*, 544–551. [CrossRef]
11. Overvig, A.; Alù, A. Diffractive Nonlocal Metasurfaces. *Laser Photonics Rev.* **2022**, *16*, 2100633. [CrossRef]
12. Gigli, C.; Li, Q.; Chavel, P.; Leo, G.; Brongersma, M.L.; Lalanne, P. Fundamental Limitations of Huygens' Metasurfaces for Optical Beam Shaping. *Laser Photonics Rev.* **2021**, *15*, 2000448. [CrossRef]
13. Hsu, L.; Dupré, M.; Ndao, A.; Yellowhair, J.; Kanté, B. Local phase method for designing and optimizing metasurface devices. *Opt. Express* **2017**, *25*, 24974–24982. [CrossRef]
14. Yao, J.; Lai, F.; Fan, Y.; Wang, Y.; Huang, S.; Leng, B.; Liang, Y.; Lin, R.; Chen, S.; Chen, M.K.; et al. Nonlocal meta-lens with Huygens' bound states in the continuum. *Nat. Commun.* **2024**, *15*, 6543. [CrossRef]
15. Malek, S.C.; Overvig, A.C.; Alù, A.; Yu, N. Multifunctional resonant wavefront-shaping meta-optics based on multilayer and multi-perturbation nonlocal metasurfaces. *Light Sci. Appl.* **2022**, *11*, 246. [CrossRef] [PubMed]
16. Adam, O.; Andrea, A. Wavefront-selective Fano resonant metasurfaces. *Adv. Photonics* **2021**, *3*, 26002.

17. Zhou, Z.; Zhang, X.; Qin, H.; Gao, Z.; Zhang, Y.; Huang, C.; Fang, F.; Lu, Y.; Kou, J. Inverse Design of Multiplexable Meta-Devices for Imaging and Processing. *ACS Photonics* **2025**, *12*, 246–252. [CrossRef]
18. Ji, A.; Song, J.; Li, Q.; Xu, F.; Tsai, C.; Tiberio, R.C.; Cui, B.; Lalanne, P.; Kik, P.G.; Miller, D.A.B.; et al. Quantitative phase contrast imaging with a nonlocal angle-selective metasurface. *Nat. Commun.* **2022**, *13*, 7848. [CrossRef]
19. Sell, D.; Yang, J.; Doshay, S.; Yang, R.; Fan, J.A. Large-Angle, Multifunctional Metagratings Based on Freeform Multimode Geometries. *Nano Lett.* **2017**, *17*, 3752–3757. [CrossRef]
20. Gershnabel, E.; Chen, M.; Mao, C.; Wang, E.W.; Lalanne, P.; Fan, J.A. Reparameterization Approach to Gradient-Based Inverse Design of Three-Dimensional Nanophotonic Devices. *ACS Photonics* **2023**, *10*, 815–823. [CrossRef]
21. Bayati, E.; Pestourie, R.; Colburn, S.; Lin, Z.; Johnson, S.G.; Majumdar, A. Inverse designed extended depth of focus meta-optics for broadband imaging in the visible. *Nanophotonics* **2022**, *11*, 2531–2540. [CrossRef]
22. Mansouree, M.; McClung, A.; Samudrala, S.; Arbabi, A. Large-Scale Parametrized Metasurface Design Using Adjoint Optimization. *ACS Photonics* **2021**, *8*, 455–463. [CrossRef]
23. Chung, H.; Miller, O.D. High-NA achromatic metalenses by inverse design. *Opt. Express* **2020**, *28*, 6945–6965. [CrossRef] [PubMed]
24. Zhang, J.; Liang, H.; Long, Y.; Zhou, Y.; Sun, Q.; Wu, Q.; Fu, X.; Martins, E.R.; Krauss, T.F.; Li, J.; et al. Metalenses with Polarization-Insensitive Adaptive Nano-Antennas. *Laser Photonics Rev.* **2022**, *16*, 2200268. [CrossRef]
25. Zhou, Y.; Mao, C.; Gershnabel, E.; Chen, M.; Fan, J.A. Large-Area, High-Numerical-Aperture, Freeform Metasurfaces. *Laser Photonics Rev.* **2024**, *18*, 2300988. [CrossRef]
26. Kanmaz, T.B.; Ozturk, E.; Demir, H.V.; Gunduz-Demir, C. Deep-learning-enabled electromagnetic near-field prediction and inverse design of metasurfaces. *Optica* **2023**, *10*, 1373–1382. [CrossRef]
27. Li, M.; Zhang, Y.; Ma, Z. Deep-Learning-Based Metasurface Design Method Considering Near-Field Couplings. *IEEE J. Multiscale Multiphys. Comput. Technol.* **2023**, *8*, 40–48. [CrossRef]
28. An, S.; Zheng, B.; Shalaginov, M.Y.; Tang, H.; Li, H.; Zhou, L.; Dong, Y.; Haerinia, M.; Agarwal, A.M.; Rivero-Baleine, C.; et al. Deep Convolutional Neural Networks to Predict Mutual Coupling Effects in Metasurfaces. *Adv. Opt. Mater.* **2022**, *10*, 2102113. [CrossRef]
29. Ma, Y.; Kolb, J.F.; Ihalage, A.A.; Andy, A.S.; Hao, Y. Incorporating Meta-Atom Interactions in Rapid Optimization of Large-Scale Disordered Metasurfaces Based on Deep Interactive Learning. *Adv. Photonics Res.* **2023**, *4*, 2200099. [CrossRef]
30. Ha, Y.; Luo, Y.; Pu, M.; Zhang, F.; He, Q.; Jin, J.; Xu, M.; Guo, Y.; Li, X.; Li, X.; et al. Physics-data-driven intelligent optimization for large-aperture metalenses. *Opto-Electron. Adv.* **2023**, *6*, 230133. [CrossRef]
31. Khoram, E.; Wu, Z.; Qu, Y.; Zhou, M.; Yu, Z. Graph Neural Networks for Metasurface Modeling. *ACS Photonics* **2023**, *10*, 892–899. [CrossRef]
32. Zhelyeznyakov, M.V.; Brunton, S.; Majumdar, A. Deep Learning to Accelerate Scatterer-to-Field Mapping for Inverse Design of Dielectric Metasurfaces. *ACS Photonics* **2021**, *8*, 481–488. [CrossRef]
33. Wu, O.; Qian, C.; Fan, Z.; Zhu, X.; Chen, H. General Characterization of Intelligent Metasurfaces with Graph Coupling Network. *Laser Photonics Rev.* **2025**, *19*, 2400979. [CrossRef]
34. Fu, R.; Deng, L.; Guan, Z.; Chang, S.; Tao, J.; Li, Z.; Zheng, G. Zero-order-free meta-holograms in a broadband visible range. *Photonics Res.* **2020**, *8*, 723–728. [CrossRef]
35. Zhang, X.; Jin, J.; Wang, Y.; Pu, M.; Li, X.; Zhao, Z.; Gao, P.; Wang, C.; Luo, X. Metasurface-based broadband hologram with high tolerance to fabrication errors. *Sci. Rep.* **2016**, *6*, 19856. [CrossRef] [PubMed]
36. Gu, M.; Cheng, C.; Zhan, Z.; Zhang, Z.; Cui, G.; Zhou, Y.; Zeng, X.; Gao, S.; Choi, D.; Cheng, C.; et al. Dielectric Supercell Metasurfaces for Generating Focused Higher-Order Poincaré Beams with the Residual Copolarization Component Eliminated. *ACS Photonics* **2024**, *11*, 204–217. [CrossRef]
37. He, G.; Zheng, Y.; Zhou, C.; Li, S.; Shi, Z.; Deng, Y.; Zhou, Z. Multiplexed manipulation of orbital angular momentum and wavelength in metasurfaces based on arbitrary complex-amplitude control. *Light Sci. Appl.* **2024**, *13*, 98. [CrossRef]
38. Ren, H.; Fang, X.; Jang, J.; Bürger, J.; Rho, J.; Maier, S.A. Complex-amplitude metasurface-based orbital angular momentum holography in momentum space. *Nat. Nanotechnol.* **2020**, *15*, 948–955. [CrossRef]
39. So, S.; Kim, J.; Badloe, T.; Lee, C.; Yang, Y.; Kang, H.; Rho, J. Multicolor and 3D Holography Generated by Inverse-Designed Single-Cell Metasurfaces. *Adv. Mater.* **2023**, *35*, 2208520. [CrossRef]
40. Xiong, B.; Liu, Y.; Xu, Y.; Deng, L.; Chen, C.; Wang, J.; Peng, R.; Lai, Y.; Liu, Y.; Wang, M. Breaking the limitation of polarization multiplexing in optical metasurfaces with engineered noise. *Science* **2023**, *379*, 294–299. [CrossRef]
41. Qu, G.; Yang, W.; Song, Q.; Liu, Y.; Qiu, C.; Han, J.; Tsai, D.; Xiao, S. Reprogrammable meta-hologram for optical encryption. *Nat. Commun.* **2020**, *11*, 5484. [CrossRef]
42. Wei, W.; Tang, P.; Shao, J.; Zhu, J.; Zhao, X.; Wu, C. End-to-end design of metasurface-based complex-amplitude holograms by physics-driven deep neural networks. *Nanophotonics* **2022**, *11*, 2921–2929. [CrossRef]
43. Pang, H.; Wang, J.; Cao, A.; Deng, Q. High-accuracy method for holographic image projection with suppressed speckle noise. *Opt. Express* **2016**, *24*, 22766–22776. [CrossRef]

44. Gao, H.; Fan, X.; Wang, Y.; Liu, Y.; Wang, X.; Xu, K.; Deng, L.; Zeng, C.; Li, T.; Xia, J.; et al. Multi-foci metalens for spectra and polarization ellipticity recognition and reconstruction. *Opto-Electron. Sci.* **2023**, *2*, 220026. [CrossRef]
45. Huo, P.; Tan, L.; Jin, Y.; Zhang, Y.; Liu, M.; Lin, P.; Zhang, S.; Wang, Y.; Ren, H.; Lu, Y.; et al. Broadband and parallel multiple-order optical spatial differentiation enabled by Bessel vortex modulated metalens. *Nat. Commun.* **2024**, *15*, 9045. [CrossRef]
46. Fröch, J.E.; Huang, L.; Zhou, Z.; Tara, V.; Fang, Z.; Colburn, S.; Zhan, A.; Choi, M.; Manna, A.; Tang, A.; et al. Full color visible imaging with crystalline silicon meta-optics. *Light Sci. Appl.* **2025**, *14*, 217. [CrossRef]